Chemosphere 314 (2023) 137720

Contents lists available at ScienceDirect

Chemosphere

journal homepage: www.elsevier.com/locate/chemosphere

Synthesis of Cu_2O micro/nanocrystals for catalytic combustion of high-concentration CO: The crucial role of glucose

Pandong Ma [a,b,1], Chenhang Zhang [a,b,1], Baojuan Dou [b], Xiaokun Yi [b], Feng Bin [a,c,*], Wenjun Liang [d,**]

[a] State Key Laboratory of High-Temperature Gas Dynamics, Institute of Mechanics, Chinese Academy of Sciences, Beijing, 100190, PR China
[b] College of Marine and Environmental Science, Tianjin University of Science & Technology, Tianjin, 30022, PR China
[c] School of Engineering Science, University of Chinese Academy of Sciences, Beijing, 100049, PR China
[d] Key Laboratory of Beijing on Regional Air Pollution Control, Beijing University of Technology, Beijing, 100124, PR China

HIGHLIGHTS

- Effects of reducing agent on catalytic properties is greater than that of copper salt.
- High concentration CO can achieve self-sustained catalytic combustion on obtained Cu_2O.
- Glucose enhances unsaturation of Cu atoms contributing to high activity.
- Chemically adsorbed oxygen on Cu_2O surface promotes CO ignition.

GRAPHICAL ABSTRACT

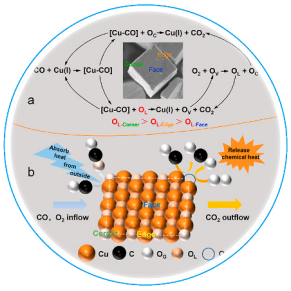

ARTICLE INFO

Handling editor: CHANG MIN PARK

Keywords:
Cu_2O micro/Nanocrystals
Carbon monoxide
Self-sustained catalytic combustion
Chemically adsorbed oxygen

ABSTRACT

Cubic Cu_2O micro/nanocrystals were successfully synthesized by liquid-phase reduction using copper salt of $CuSO_4$ or $CuCl_2{\cdot}2H_2O$, and glucose or ascorbic acid as reducing agent, respectively. The activity of the catalysts was evaluated by light-off curves of CO self-sustained catalytic combustion via temperature-programmed oxidation of CO (CO-TPO), with the results showing the activity of catalysts following the order of Cu_2O–Cl-GLU > Cu_2O–*S*-GLU > Cu_2O–*S*-AA > Cu_2O–Cl-AA, (Cl denotes $CuCl_2{\cdot}2H_2O$, GLU denotes glucose, S denotes $CuSO_4$ and AA denotes ascorbic acid, respectively), corresponding to the ignition temperature of 109 °C, 122 °C, 137 °C and 186 °C, respectively. The crystal structure, elemental valence, morphology and redox property of the prepared catalysts were analyzed by using various characterization techniques. Combined with in situ infrared spectrum, the CO self-sustained catalytic combustion over Cu_2O catalysts mainly follows the Mars-van-Krevelen (M-v-K) mechanism: the adsorbed and activated CO reacts with lattice oxygen to yield CO_2 and oxygen vacancy, and then the oxygen vacancy can be replenished by gaseous oxygen. Combined with catalytic performance of high-concentration CO, it is found that the catalysts prepared using glucose as reducing agent are more angular compared with ascorbic acid. The Cu_2O–Cl-GLU synthesized with glucose and $CuCl_2{\cdot}2H_2O$ exhibits the best

* Corresponding author. State Key Laboratory of High-Temperature Gas Dynamics, Institute of Mechanics, Chinese Academy of Sciences, Beijing, 100190, PR China.
** Corresponding author.
E-mail addresses: binfeng@imech.ac.cn (F. Bin), liangwenj@bjut.edu.cn (W. Liang).
[1] Pandong Ma and Chenhang Zhang contributed equally to this work.

https://doi.org/10.1016/j.chemosphere.2022.137720
Received 8 November 2022; Received in revised form 12 December 2022; Accepted 29 December 2022
Available online 31 December 2022

catalytic activity among all the catalysts tested, attributing to its more obvious edge and rough crystal surface. The unique structure of Cu_2O–Cl-GLU leads to the high exposure rate and coordination unsaturation of atoms on the cubic Cu_2O micro/nanocrystals that can improve the ability of activating gaseous O_2 and low temperature reducibility, and consequently facilitating the catalytic activity.

1. Introduction

The emergence of energy crisis has triggered awareness focused on the clean and efficient utilization of energy and explores new ways to improve the utilization rate of existing energy and waste energy (Kang et al., 2021; Bin et al., 2015, 2019). In the field of steel-making field, a large amount of off-gas containing high concentration CO is often discharged into atmosphere by methane combustion in the exhaust tower, leading to serious energy waste. Such a simple treatment can also generate secondary pollutant of thermal NO_x, and lost the sensible heat of off-gas and chemical heat of CO that should have been recovered. This awkward problem can be solved if the high concertation of CO in the steel-making off-gas can be employed as fuel with medium calorific value, and then the recycling, as an alternative strategy to methane combustion-supporting flare burners, exhibits high economic value (Bin et al., 2015, 2019; Kang et al., 2020).

The catalytic combustion has been proved as an effective method to the treatment and recycling of the released gas of steel-making (Kang et al., 2018, 2020, 2021; Bin et al., 2015, 2019; Ma et al., 2021). A high level of CO can be ignited over a catalyst under a $CO/O_2/N_2$ atmosphere. When the catalytic converter warms up to its ignition temperature, the sudden self-acceleration of the surface rate leads to a thermochemical runaway, followed by a rapid transition to self-sustained catalytic combustion. Copper-based heterogeneous catalysts are used as an alternative to noble metals. In recent years, benefiting from the rapid development of inorganic synthesis, nano-structured Cu_2O materials with rational shape control and superior redox properties have been synthesized, which exhibits good application prospects in many research fields, such as CO oxidation reaction, photocatalytic reaction (Liu et al., 2013; Jiang et al., 2017; Muthukumaran et al., 2019; Shang et al., 2012), solar cell (Xu et al., 2018), gas sensing material (Wu et al., 2016), photocathode material (Qin et al., 2022) and so on (Bao et al., 2011; Feng et al., 2014; Yoon et al., 2015; Li et al., 2013; Zhang et al., 2019a, Zhang et al., 2019b; Karapetyan et al., 2015; Ng and Ngan, 2013; Ahmed et al., 2021; Shi et al., 2012; Fan et al., 2012).

The synthesis methods of Cu_2O micro/nanocrystals include solid-phase method, liquid-phase method (Luo et al., 2015) and electro-reduction method (Yoon et al., 2015), etc (Liu et al., 2013; Feng et al., 2014; Karapetyan et al., 2015; Ng and Ngan, 2013; Zhu et al., 2011; Kumar et al., 2016; Yang et al., 2017). The Cu_2O prepared by liquid phase reduction method has several advantages such as easy regulation of morphology and good particle size uniformity (Ma et al., 2021; Li et al., 2013; Zhu et al., 2011; Chang et al., 2013; Liang et al., 2009), where the process of preparing Cu_2O by liquid phase reduction is simple and can be divided into the following steps. A certain amount of NaOH is added into the copper salt precursor solution at a certain temperature, then the copper species precipitate in the form of $Cu(OH)_2$. After a period of time, a certain amount of weak reducing agent is added to reduce $Cu(OH)_2$ to Cu_2O (Chang et al., 2013). Generally, copper salt precursors include $CuSO_4$, $CuCl_2$, $Cu(NO_3)_2$, $Cu(CH_3COO)_2$, etc. (Bao et al., 2011; Li et al., 2013; Hua et al., 2013, 2014), and weak reducing agents include glucose, ascorbic acid, xylitol, etc (Shang et al., 2012; Ghosh et al., 2016). Our previous studies (Ma et al., 2021) have found that changing the concentration of precursor can effectively adjust the morphology of Cu_2O micro/nanocrystals catalyst, exposing more active crystal planes and thus decreasing the ignition temperature of CO. Besides, the morphology, physicochemical properties and catalytic performance of the catalyst may also be related to the types of copper salt precursors (Park et al., 2009) and reducing agents (Shang et al., 2012; Ghosh et al., 2016), and in this case the excellent activity optimized is beneficial for practical application.

In this study, the copper salts ($CuCl_2{\cdot}2H_2O$ or $CuSO_4$) and reducing agents (ascorbic acid or glucose) were used as precursors to prepare Cu_2O micro/nanocrystals catalysts. The activity of the catalysts was evaluated by light-off curves of CO self-sustained catalytic combustion via temperature-programmed oxidation of CO (CO-TPO). The crystal structure, element valence and crystal morphology of the catalysts were analyzed by conventional characterization technologies, such as X-ray powder diffraction (XRD), X-ray photoelectron spectroscopy (XPS) and scanning electron microscopy (SEM). Through temperature-programmed reduction of H_2 (H_2-TPR), temperature-programmed desorption of O_2 (O_2-TPD), temperature-programmed desorption of CO coupled with mass spectrum (CO-TPD-MS) experiments, the relationship between catalytic activity and the reducibility, adsorption of reaction gas and the difficulty of lattice oxygen (O_L) participating in CO oxidation are analyzed here, and then the activity induced by the sensitivity of catalyst structure is pointed out in detail. This paper provides the outstanding contribution here: the reducing agent of glucose can promote the formation of sharper edges and corners, and $CuCl_2{\cdot}2H_2O$ can attribute to the rough crystal surface of cubic Cu_2O micro/nanocrystals, which leads to the high exposure rate and coordination unsaturation of atoms on the catalyst surface. In this case, abundant lattice oxygen that activates gaseous O_2 in the sharp edges, corner of Cu_2O micro/nanocrystals are the main reasons for the improvement of the CO oxidation. These results obtained are conducive to the accurate design of catalyst surface/interface structure and the clean/efficient utilization of waste energy.

2. Experimental section

2.1. Catalyst preparation

$CuCl_2{\cdot}2H_2O$, $CuSO_4$, NaOH, ascorbic acid and glucose are provided by Sinopharm Chemical Reagent Co. (PR China), which were used directly in the following experiment. The schematic diagram of catalyst preparation process is shown in Scheme 1. 0.01 mol of copper salt ($CuCl_2{\cdot}2H_2O$ or $CuSO_4$) was dissolved in 1 L of ultrapure water, and stirred at 55 °C for 30 min at constant temperature. Then 100 mL of NaOH (2 mol/L) and 100 mL of ascorbic acid solution (0.6 mol/L) or glucose solution formed by dissolving 34.2 g of glucose in 300 mL of ultrapure water were added in the reaction system. After stirring at constant temperature for 5 h, dark red powder precipitates were gradually formed in the mixed system. The powder solid catalyst was obtained after centrifugal washing for 5 times, and vacuum drying at 60 °C overnight. The catalysts prepared with ascorbic acid using $CuCl_2{\cdot}2H_2O$ and $CuSO_4$ were recorded as Cu_2O–Cl-AA and Cu_2O–*S*-AA, respectively. The catalysts prepared with glucose using $CuCl_2{\cdot}2H_2O$ and $CuSO_4$ were identified as Cu_2O–Cl-GLU and Cu_2O–*S*-GLU, respectively. As shown in Scheme 1, Cu_2O micro/nanocrystals are formed in an alkaline liquid environment, and the growth and formation process can be described by the following equations:

$$Cu(II) + 2OH^- \rightarrow Cu(OH)_2 \quad (1)$$

$$2Cu(OH)_2 + C_6H_8O_6 \rightarrow Cu_2O + C_6H_6O_6 + 3H_2O \text{ (Chang et al., 2013)} \quad (2)$$

$$2Cu(OH)_2 + C_6H_{12}O_6 \rightarrow Cu_2O + C_6H_{10}O_6 + 3H_2O \quad (3)$$

When ascorbic acid is employed as reducing agent, the reaction follows the reaction processes of (1) and (2). When glucose is used as a

reducing agent, the reaction follows the reaction processes of (1) and (3).

2.2. Characterization

Powder X-ray diffraction (XRD) measurements were performed with a Rigaku Smart Lab SE Automated Multipurpose X-ray Diffractometer using the Cu Kα radiations (λ = 1.54059 Å) with a scanning speed of 2°/min. The chemical state and surface components of the catalysts was analyzed by X-ray photoelectron spectroscopy (XPS) on a PerkinElmer PHI-1600 using Mg Kα excitation. The reference binding energy was chosen to match the C1s binding energy of electrons in alkyl group equal to 284.8 eV. The particle size and morphologies of the catalysts were obtained by field emission scanning electron microscope (SEM, Gemini SEM 300). Temperature-programmed reduction of hydrogen (H_2-TPR) and temperature programmed-desorption of oxygen (O_2-TPD) were carried out on a TP5080B chemisorption analyzer. With respect to H_2-TPR, each sample (15 mg) was first treated at 300 °C for 30 min in N_2 and cooled to room temperature in the same atmosphere, then swept with 5% H_2/Ar mixture (30 mL min^{-1}) until the base line on the recorder remained unchanged. Finally, the sample was heated at a rate of 10 °C min^{-1} to record the TPR spectra. The amount of H_2 consumed for the reduction was measured with a thermal conductivity detector (TCD). For O_2-TPD, each sample (50 mg) was heated in a N_2 flow of 30 mL min^{-1} and maintained at 300 °C for 30 min. After that, an air (O_2/N_2 (1: 4)) flow of 30 mL min^{-1} was switched to purge the sample for 30 min. Finally, the O_2-TPD experiment was carried out by increasing the temperature (10 °C min^{-1}) up to 1000 °C. The temperature-programmed desorption of CO (CO-TPD) is also carried out on the TP5080B chemisorption analyzer, and the quadrupole mass spectrometer (Pfeiffer PrismaPlus) is connected at the exhaust port. High purity CO was adsorbed on the sample for 30 min at room temperature and then was exposed to Ar. After the baseline was stable (about 30min), the reactor was heated at a rate of 10 °C min^{-1} until reaching 600 °C and the TPD spectra were taken with the mass spectrometer. In-situ infrared spectrum was collected by the FOLI10-R instrument (INSA Optics Instruments (Shanghai) Ltd.) coupled with a self-designed magnetically driven transmission cell, where approximately 5 mg of catalyst and 50 mg KBr were mixed and pressed into a self-supporting wafer. Prior to recording IR spectra, the sample was pretreated in an Ar flow at 500 °C.

2.3. Catalytic activity test

The catalytic activity evaluation was carried out in a fixed bed reactor (Ma et al., 2021; Kang et al., 2020). Specifically, 50 mg of fresh catalyst and 50 mg of quartz sand were evenly mixed, loaded into a quartz tube reactor, and pretreated in a high-purity Ar atmosphere at 300 °C for 1 h to blow out impurities. A constant feed composition was used with 10% CO, 21% O_2, and 69% N_2 as balance. The flow rate was 0.2 L min^{-1} and the gas hourly space velocity (GHSV) of the reaction was maintained at 60,000 h^{-1}. Online gas analyzer (QGS-08C for CO/CO_2 and OGS-10 T for O_2, Maihak) was used to monitor the outlet concentration of CO, O_2 and CO_2. A K-type thermocouple was inserted into the catalyst bed to monitor the internal temperature. During each temperature programmed oxidation run, the heating rate was set at 10 °C min^{-1}. The conversion rate of CO was obtained by the average of three experiments, and it was calculated as

$$C_{CO} = \frac{[CO]_{in}\% - [CO]_{out}\%}{[CO]_{in}\%} \quad (4)$$

where C_{CO} is the CO conversion rate, $[CO]_{in}$ is the CO concentrations in inlet gas and $[CO]_{out}$ is the CO concentrations in outlet gas. R_{CO} was used to calculate the reaction rate via the following equation:

$$R_{CO} = \frac{N_{CO} \times C_{CO}}{W_{cat}} \quad (5)$$

where R_{CO} is the reaction rate in $mol_{CO}/(g_{cat} \cdot s)$, N_{CO} is the CO molar gas flow rate in mol/s and W_{cat} is the catalyst weight in grams. The temperature distributions of the reactor surface were detected by a forward-looking infrared radiometer (FLIR, T640, USA) after realizing CO self-sustained combustion, with a certain glass emission rate (0.87).

3. Results and discussion

3.1. CO self-sustained catalytic combustion

Fig. 1a shows the light-off curves of CO self-sustained catalytic combustion using Cu_2O-Cl-AA, Cu_2O–*S*-AA, Cu_2O–*S*-GLU and Cu_2O–Cl-GLU catalysts, considering the heating and cooling feeding conditions, respectively. Upon the heating feeding, the catalytic ignition of CO is a complex process including kinetics and heat generation because the heat produced is governed by the reaction rate, which in turn is determined by the reaction kinetics. Correspondingly, a transition from low-reactivity steady state to high-reactivity steady state can be observed due to heat transfer limitation, which exhibits different reaction processes. Take the Cu_2O–Cl-GLU for example, the first step can be described as a slow induction process that begins at 60 °C and then continues, at a relatively slow rate until 108 °C. Here the temperature of catalyst bed close to the controlled temperature suggests that the reaction is kinetically controlled. The second step is the ignition process induced at gas–solid phase interface, with the reaction rate determined by internal diffusion. The CO oxidation rate is so fast as to induce a strong increase of the local temperature which consequently accelerates the external diffusion and mass-transfer. The third phase concerns temperatures well above the ignition region, corresponding to CO conversion rate reaching 100%. Entering this step means the reaction rate becomes controlled by external diffusion. As such, when the furnace stops heating but the CO conversion rate is maintained at 100% without obvious decrease for several hours. Such a phenomenon is called as CO self-sustained catalytic combustion since the heat loss of the reaction system and the temperature of CO catalytic combustion are well maintained when the chemical heat is released by the complete oxidation of CO.

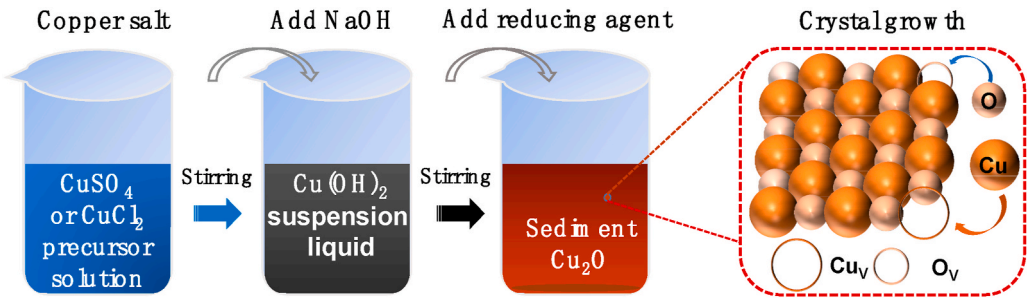

Scheme 1. Schematic diagram of catalyst preparation process.

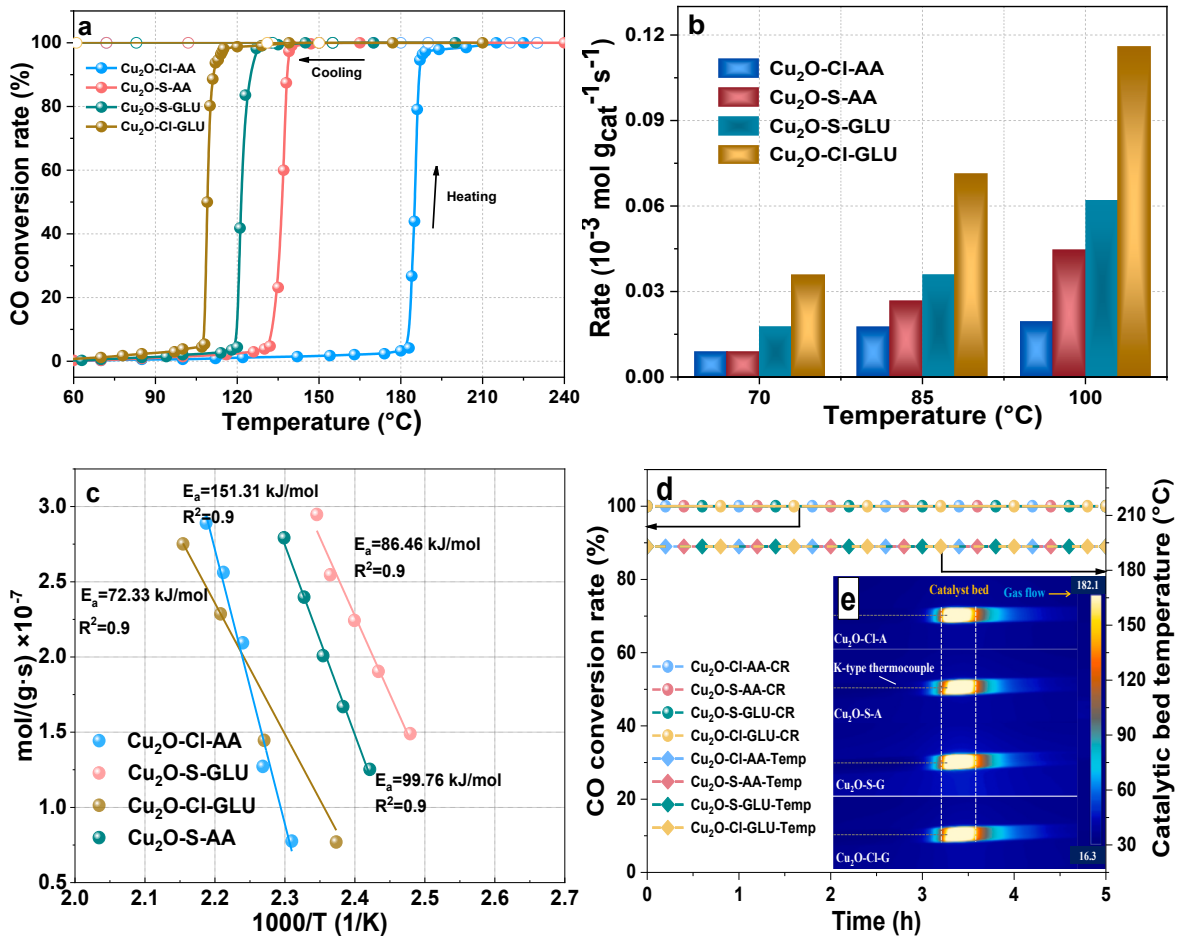

Fig. 1. Light-off curves of CO self-sustained catalytic combustion over Cu_2O–Cl-AA, Cu_2O–*S*-AA, Cu_2O–*S*-GLU and Cu_2O–Cl-GLU catalysts (a), and the CO reaction rate of catalysts calculated at different temperatures (b). Constant feed composition: 10% CO+21% O_2/N_2. The flow rate was 0.2 L min^{-1} and the GHSV was maintained at 60,000 h^{-1}. CO activity analyzed in the kinetic regime with a converted rate of less than 10%. Constant feed composition: 1% CO+21%O_2/N_2 (c). CO conversion rate and catalyst bed temperature within 5 h (d), and the embedded images as the temperature field of the outer wall of reactors (e). Constant feed composition: 10% CO + 21% O_2/N_2. The flow rate was 0.2 L min^{-1} and the GHSV was maintained at 60,000 h^{-1}. The conversion rate and catalyst bed temperature are abbreviated as CR and Temp, respectively.

Upon the cooling feeding (Fig. 1a), the conversions of CO for all the catalysts tested maintain 100% when the furnace temperature decreasing to 60 °C by 10 °C min^{-1} cooling rate, indicating that CO self-sustained catalytic combustion system cannot be interfered from external temperature. The lower the temperature required to achieve the same CO conversion, the better the activity of catalysts. Here, the ignition temperature is defined as the temperature (T_i) for which 50% CO conversion is achieved, corresponding to T_i of 109 ± 2 °C, 122 ± 2 °C, 137 ± 2 °C and 186 ± 2 °C for Cu_2O–Cl-GLU, Cu_2O–*S*-GLU, Cu_2O–*S*-AA, Cu_2O–Cl-AA, respectively. Among them, the T_i temperature of Cu_2O–Cl-GLU with the best activity is about 77 °C lower than that of Cu_2O–Cl-AA with the worst activity. Meanwhile, compared with the relevant samples reported in the literature, Cu_2O–Cl-GLU catalysis has the better activity those of the related samples reported in the literature shown in Table 1. Fig. 1b shows the relationship between reaction rate and temperature. Under the same temperature, faster reaction rate suggests better activity of catalysts. Obviously, the reaction rates increase with temperature. At a temperature of 70 °C, the reaction rates of Cu_2O–Cl-GLU and Cu_2O–*S*-GLU are higher than those of Cu_2O–Cl-AA and Cu_2O–*S*-AA. Meanwhile, the reaction rate of Cu_2O–Cl-GLU was higher than that of Cu_2O–*S*-GLU. With further increasing the temperature, the order of CO reaction rate over catalysts decreases, following the order of Cu_2O–Cl-GLU > Cu_2O–*S*-GLU > Cu_2O–*S*-AA > Cu_2O–Cl-AA, and this trend becomes more and more obvious with temperature. Energy activation values calculated via oxidation of CO vs temperature curves reflect the catalyst activity, with the Arrhenius plot shown in Fig. 1C. The data was selected under conditions in which CO conversion was less than 10% to minimize the effect of mass and heat transfer. The energy activation values decreased in the following order: Cu_2O–Cl-GLU (72.33 kJ mol^{-1}) > Cu_2O–*S*- GLU (86.46 kJ mol^{-1}) > Cu_2O–*S*-AA (99.76 kJ mol^{-1}) > Cu_2O–Cl-AA (151.13 kJ

Table 1
The ignition temperature (T_{10}) of CO oxidation over different catalysts under different reaction conditions.

Samples	Reaction gas mixture	GHSV (h^{-1})	T_{10} (°C)	Reference
$LaCoO_3$	1% CO + 2%O_2/N_2	30,000	181	Yang et al. (2022)
Cu_2O-9	10% CO + 21%O_2/N_2	60,000	113	Ma et al. (2021)
Cu_2O-5	10% CO + 21%O_2/N_2	60,000	110	Ma et al. (2021)
AgCeO	1% CO + 5%O_2/N_2	30,000	120	Rao et al. (2022)
Cu_2O-1	10% CO + 21%O_2/N_2	60,000	102	Ma et al. (2021)
Cu_2O	5% CO + 21%O_2/N_2	30,000	182	Kang et al. (2022)
Cu_2O–Cl-GLU	10% CO + 21%O_2/N_2	60,000	107	This work

mol^{-1}). Predictably, the Cu_2O–Cl-GLU with the lowest energy activation has the best catalytic activity for CO oxidation, consistent with the above activity results.

Fig. 1d shows the stable combustion activity of all the catalysts tested. The CO conversion and the axis temperature of catalyst bed do not decrease within 5 h during self-sustaining catalytic combustion (measured by extending the thermocouple into the catalyst bed), exhibiting the good stability of Cu_2O (Fig. 1d). Fig. 1e displays the two-dimensional temperature distribution of CO self-sustaining catalytic combustion process on the outer wall of the reactors. The maximum temperature (bright yellow) is about 182 °C, and the minimum temperature (dark blue) is about 16 °C. Due to heat and mass transfer, there can be a large amount of heat loss on the outer surface of reactor, resulting in the fact that the experimental value (182 °C) observed by thermal imager is lower than that fed back by thermocouple (193 °C). It can be also seen from Fig. 2b that the temperature of catalyst bed for all the catalysts tested maintains almost the same values during CO self-sustaining catalytic combustion, suggesting that the combustion system runs in a stable state.

3.2. Structure and chemical states

Fig. 2 shows the XRD patterns of Cu_2O–Cl-AA, Cu_2O–*S*-AA, Cu_2O–*S*-GLU and Cu_2O–Cl-GLU catalysts, with the 2θ angles at 29.57°, 36.42°, 42.31°, 62.46°, 73.52° and 77.37° exhibited corresponding to (110), (111), (200), (211), (311) and (222) crystal planes of Cu_2O (JCPDS No. 99–0041) respectively, indicative of standard cubic phase crystal structure (Bao et al., 2011; Zhang et al., 2019a; Shang et al., 2012). The peaks display sharp without other impurity peaks, indicating that the prepared Cu_2O crystal exhibits high crystallinity and purity. Cu_2O–*S*-GLU has the highest relative intensity, which proves that the (111) crystal planes of Cu_2O are abundant. The low crystallinity of Cu_2O–Cl-AA leads to a weaker relative content of the (111) crystal planes of Cu_2O and a lower half-height width at 42.21°. Furthermore, the average crystallite size of the catalysts nanoparticles is ~1.3 μm based on the Debye–Scherrer equation. Considering the characteristic diffraction peak of XRD pattern with higher intensity leading to higher crystallinity of the catalyst crystal, the order of crystallinity of all the catalysts is Cu_2O–*S*-GLU > Cu_2O–*S*-AA > Cu_2O–Cl-GLU > Cu_2O–Cl-AA.

The chemical states and surficial compositions of catalysts are investigated by XPS. Fig. 3a shows the XP spectra of Cu 2p for the catalysts, with characteristic diffraction peaks at 952.7eV and 932.7eV binding energies belonging to Cu $2p_{1/2}$ and Cu $2p_{3/2}$, respectively (Bao et al., 2011; Zhang et al., 2019b; Hua et al., 2013). No characteristic peaks and satellite peaks of Cu^0 species and Cu^{2+} species are observed, suggesting that all the catalysts are pure Cu_2O. Fig. 3b shows the XP spectra of O 1s for the Cu_2O–Cl-AA, Cu_2O–*S*-AA, Cu_2O–*S*-GLU and Cu_2O–Cl-GLU catalysts. The oxygen species can be divided into chemically adsorbed oxygen (O_C), hydroxyl oxygen (O_{OH}) and lattice oxygen (O_L), located at 532.7, 531.8 and 530.7 eV, respectively (Kang et al., 2018; Xu et al., 1999; da Rosa et al., 2019). Table 2 displays the simi-quantitative analysis of element ratio on the catalyst surface. The proportion of O_C on the surface of Cu_2O–Cl-GLU exhibits the highest values, accounting for 16.3% of all oxygen species. The O_C/O on the

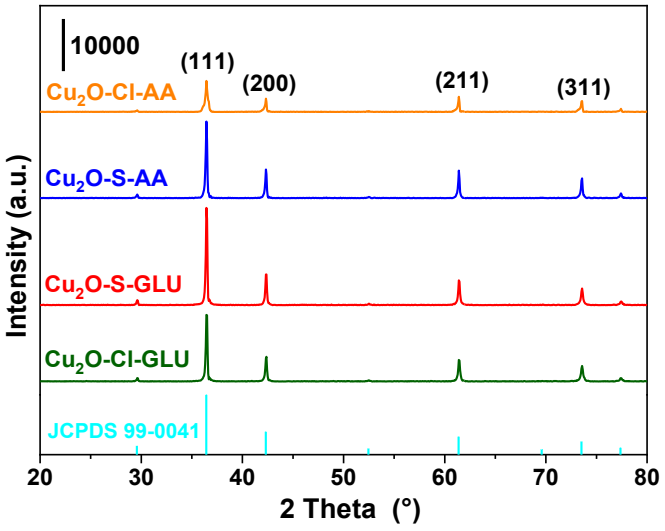

Fig. 2. XRD patterns of Cu_2O–Cl-AA, Cu_2O–*S*-AA, Cu_2O–*S*-GLU and Cu_2O–Cl-GLU catalysts.

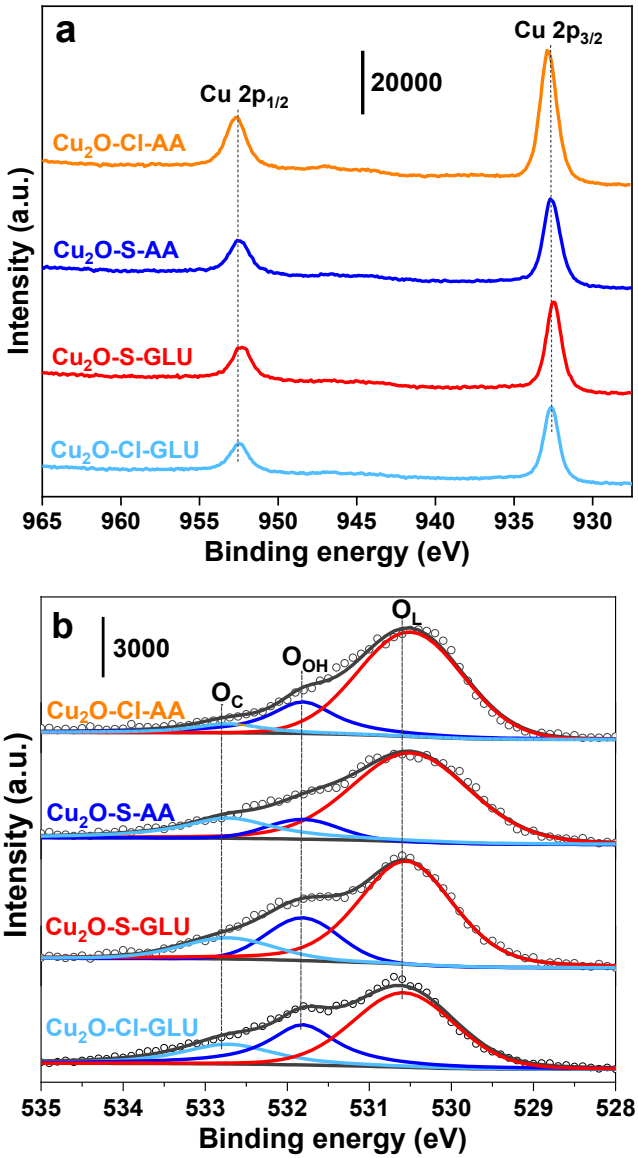

Fig. 3. XPS spectra of Cu 2p (a) and O 1s (b) of Cu_2O–Cl-AA, Cu_2O–*S*-AA, Cu_2O–*S*-GLU and Cu_2O–Cl-GLU catalysts.

Table 2
Surface atomic ratios of catalysts obtained by XPS simi-quantitative analysis.

Catalysts	O_C/O (%)	O_{OH}/O (%)	O_L/O (%)	Cu/O (%)
Cu_2O–Cl-AA	4.8	18.2	77.0	148.0
Cu_2O–*S*-AA	13.7	11.8	74.5	99.5
Cu_2O–*S*-GLU	15.4	21.2	63.4	87.7
Cu_2O–Cl-GLU	16.3	27.2	56.5	85.1

surface of Cu_2O–Cl-AA exhibits the lowest values among the catalysts tested, accounting for 4.8%. Then the O_C/O for all the catalysts decreases following the order of Cu_2O–Cl-GLU > Cu_2O–*S*-GLU > Cu_2O–*S*-AA > Cu_2O–Cl-AA. However, the O_L/O increases in the order of Cu_2O–Cl-GLU < Cu_2O–*S*-GLU < Cu_2O–*S*-AA < Cu_2O–Cl-AA, where less O_L corresponds to more oxygen vacancies and the order of coordination unsaturation. The CO catalytic activity is positively correlated with the content of chemically adsorbed oxygen on the catalyst surface, due to more oxygen vacancies existing on the surface of Cu_2O prepared with glucose as reducing agent than ascorbic acid as reducing agent, which enhances the adsorption and activation of gas-phase oxygen and thus improves its catalytic activity for CO oxidation. In particular, it can be found that the Cu/O ratio for Cu_2O–Cl-AA, Cu_2O–*S*-AA, Cu_2O–*S*-GLU and Cu_2O–Cl-GLU are 148.0%, 99.5%, 87.7% and 85.1%, respectively. During the induction process, the copper sites are the adsorption sites for the adsorption and activation of CO molecules. CO adsorption on the copper sites dominates over O_2 adsorption, i.e., self-poisoning of CO. In this case, the adsorption of O_2 on the catalysts, as the rate determining step of CO oxidation during the induction process, tend to be more difficult than that of CO. Both adsorbed CO and O_2 react to form CO_2 release.

3.3. Morphology

Fig. 4 shows SEM images of Cu_2O–Cl-AA, Cu_2O–*S*-AA, Cu_2O–Cl-GLU and Cu_2O–*S*-GLU catalysts. The cubic Cu_2O micro/nanocrystals catalysts exposing six (100) crystal planes can be prepared with $CuCl_2{\cdot}2H_2O$ or $CuSO_4$ as copper salt, ascorbic acid or glucose as reducing agent (Yoon et al., 2015; Hua et al., 2013, 2014). In addition, the crystal planes of Cu_2O prepared with ascorbic acid as reducing agent are relatively smooth and the edges and corner are relatively blunt. Nevertheless, Cu_2O prepared with glucose as reducing agent has sharp edges, corner and slightly rough crystal surface. The reason may be that the Cu_2O nanocrystals underwent in situ surface oxidation to form CuO films during CO oxidation (Zhang et al., 2019a). The reducing agent glucose enhances the edge site/surface site density, making it easier for Cu^{2+} located at the sharp edges to be reduced to Cu^{+}, thus promoting catalytic activity. It is obvious that the microstructure of Cu_2O micro/nanocrystals is not sensitive to the type of copper salt precursor, but the different types of reducing agent can influence its microstructure (see Fig. 5).

According to the results of activity test, the catalyst prepared with glucose as reducing agent exhibits the higher CO catalytic activity than that of the catalyst with ascorbic acid as reducing agent. Combined with the SEM results, Cu_2O–Cl-GLU with obvious edge and rough crystal surface has the higher activity. Taking Cu_2O–Cl-GLU with the highest activity and Cu_2O–Cl-AA with the worst activity for example, the Cu_2O–Cl-GLU seems to add active sites at edges and corner based on the active sites of Cu_2O–Cl-AA. Here, the 12 edges of the cube can be abstracted into one-dimensional Cu_2O nanowires. It is known that the atomic exposure rate and coordination unsaturation of one-dimensional

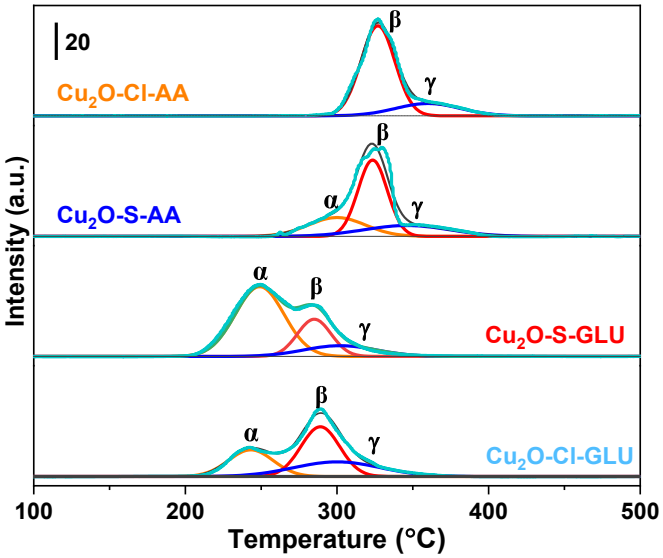

Fig. 5. H_2-TPR profiles of the Cu_2O–Cl-AA, Cu_2O–*S*-AA, Cu_2O–*S*-GLU and Cu_2O–Cl-GLU catalysts. Weight of sample: 15 mg; Gas composition and flow rate: 5% H_2/Ar mixture (30 mL min^{-1}); Heating rate: 10 °C min^{-1}.

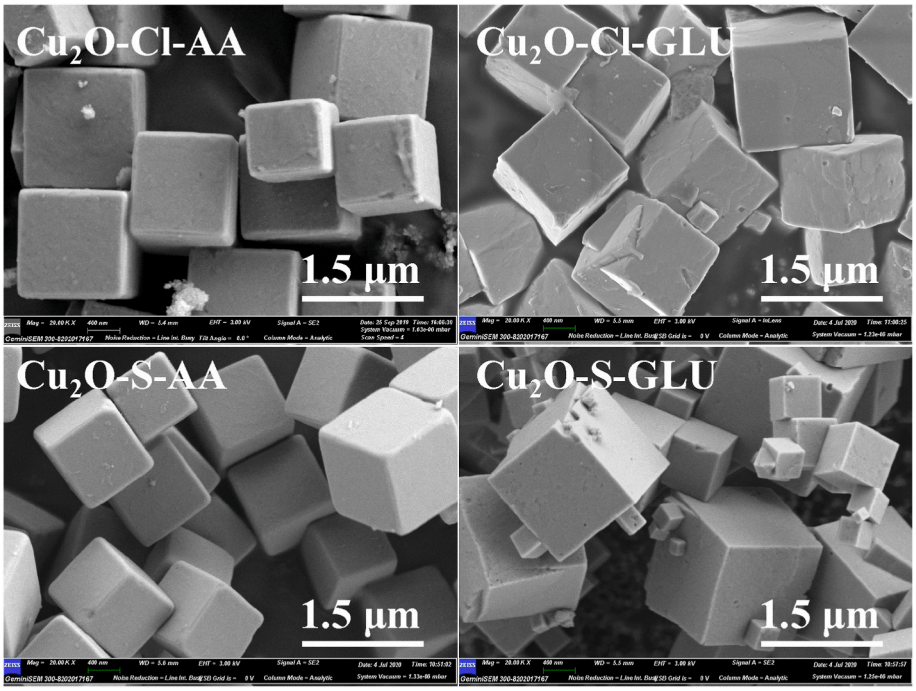

Fig. 4. SEM images of Cu_2O–Cl-AA, Cu_2O–*S*-AA, Cu_2O–Cl-GLU and Cu_2O–*S*-GLU catalysts.

nanomaterial are much higher than that of two-dimensional nanomaterial, and two-dimensional nanomaterials are much higher than that of three-dimensional bulk materials (Shang et al., 2020; Ji et al., 2020; Jiao et al., 2019). Generally, the higher atomic exposure rate and coordination unsaturation lead to the higher atomic utilization rate of catalysts and better catalytic activity. These phenomena can well explain the highest activity of Cu_2O–Cl-GLU.

3.4. Temperature-programmed thermal analysis

The redox behavior of the Cu_2O–Cl-AA, Cu_2O–*S*-AA, Cu_2O–*S*-GLU and Cu_2O–Cl-GLU catalysts has been investigated by H_2-TPR, with the results shown in Figp. 5. During the temperature programmed process, H_2 combines with O_L in Cu_2O to yield H_2O and then form oxygen vacancies (O_V), and thus the reducibility of Cu_2O is positively correlated with the O_L shedding. By fitting the H_2-TPR spectra of the four catalysts, except Cu_2O–Cl-AA with only β, γ two peaks, the other three catalysts can be fitted with α, β, γ peaks, indicating that the reduction is no longer confined to the surface of the material, but extends deep into its bulk, which may accelerate the reduction process and consume more hydrogen. Table 3 lists the peak temperature and hydrogen consumption corresponding to each reduction peak of the catalysts. The redox performance of catalysts depends mainly on their reduction temperature rather than on hydrogen consumption. The Cu_2O–Cl-GLU exhibits the α peak at the lowest temperature of 242 °C during H_2-TPR although its H_2 consumption ($\alpha + \beta + \gamma = 4.50$ mmol/g) is lower than that of Cu_2O–*S*-GLU (5.60 mmol/g), exhibiting the highest excellent reducibility among all the catalysts tested.

By comparing the temperature of the reduction peak of each catalyst, the source of the reducibility of catalysts can be inferred. For Cu_2O–Cl-AA and Cu_2O–*S*-AA, the reduction temperatures of β peaks are 326 °C and 324 °C respectively, with γ the peak reduction temperatures of 360 °C and 352 °C. Obviously, the temperature difference is within 10 °C suggests that the Cu_2O–Cl-AA and Cu_2O–*S*-AA have similar reducing sites on the catalyst surface. Combined with the SEM results, both Cu_2O–Cl-AA and Cu_2O–*S*-AA mainly expose (100) crystal planes, indicating that their reducibility mainly comes from the reduction of O_L at (100) crystal planes. The reduction temperature of Cu_2O–Cl-GLU and Cu_2O–*S*-GLU is lower than that of Cu_2O–Cl-AA and Cu_2O–*S*-AA. Similarly, the reduction β peak of Cu_2O–Cl-GLU and Cu_2O–*S*-GLU can be attributed to the reduction of O_L on the (100) crystal planes of Cu_2O micro/nanocrystals cube surface. Generally, the increase of catalyst surface defects is beneficial to improving catalyst activity (Jiang et al., 2018). For Cu_2O–Cl-GLU and Cu_2O–*S*-GLU, the increase of irregular defect sites on the crystal surface, such as step surface and concave surface, can explain why the temperature of reduction peaks (α, β and γ) decreases, compared with Cu_2O–Cl-AA and Cu_2O–*S*-AA. Therefore, for Cu_2O–Cl-GLU and Cu_2O–*S*-GLU, it can be determined that the α peak comes from the reduction of O_L exposed at the edges and corner of Cu_2O micro/nanocrystals cube. Especially for Cu_2O–Cl-GLU, the lower reduction temperature of α peak (242 °C), that is, the higher O_L activity at the edges and corner of the surface leads to further improving the activity of CO oxidation.

O_2-TPD can detect the adsorption strength and capacity of catalysts for gaseous oxygen, as shown in Fig. 6, and the desorption curve of O_2-TPD from low to high temperature is as follows: the desorption of physically adsorbed oxygen (O_P) (room temperature to 200 °C), the desorption of chemically O_C (200–700 °C) and the desorption of O_L (above 700 °C). The difference of the amount of chemisorbed oxygen among different samples as shown in Table 4. The Cu_2O–*S*-GLU and Cu_2O–Cl-GLU catalysts have abundant in O_L and O_c, while Cu_2O–Cl-GLU has the highest total amount of oxygen species among all the catalysts tested. As can be seen from Fig. 6, there is almost no chemisorbed oxygen in the O_2-TPD curve of Cu_2O–Cl-AA, which indicates that the (100) crystal of Cu_2O exhibits weak adsorption on O_2, consistent with the reference of Ma et al. (2021). The O_C desorption is observed obviously for the Cu_2O–*S*-AA, Cu_2O–*S*-GLU and Cu_2O–Cl-GLU, indicating that the adsorption of O_2 on them is better than that of Cu_2O–Cl-AA, which is agreement with that of XPS analysis of O 1s.

Fig. 7 shows the CO-TPD-MS profiles of catalysts. Almost all of the CO molecules adsorbed on the catalyst surface desorbed as CO_2 during the heating cycle without remaining CO signal detected. Hence the position and area of CO_2 desorption peak are correlated with the difficulty of CO_2 desorption and the CO adsorption capacity. Specifically, the lower peak temperature demonstrates the easier desorption of adsorbed CO in the form of CO_2, and larger peak area indicates more CO_2 is desorbed at this temperature region. The total CO_2 desorption peak areas of Cu_2O–*S*-GLU and Cu_2O–Cl-GLU are larger than those of Cu_2O–Cl-AA and Cu_2O–*S*-AA, which confirms that more CO adsorption binding sites on the surfaces of Cu_2O–*S*-GLU and Cu_2O–Cl-GLU than those of Cu_2O–Cl-AA and Cu_2O–*S*-AA. Besides, the temperature of CO_2 desorption peak (α peak) for Cu_2O–*S*-AA is lower than that of Cu_2O–Cl-AA, which suggests that some O_L on the surface of Cu_2O–*S*-AA catalyst is easy to be reduced by CO to form CO_2, and also indicates that the CO oxidation activity of Cu_2O–*S*-AA is higher than that of Cu_2O–Cl-AA. Although the amount of highly active lattice oxygen belonging to the α peak is relatively small, its role in the ignition stage of high concentration CO cannot be ignored due to the fast rate of CO exothermic reaction (Kang et al., 2021; Bin et al., 2015). Similarly, the CO oxidation activity of Cu_2O–Cl-GLU is higher than that of Cu_2O–*S*-GLU. As such, the properties of CO adsorption and activation for all the catalysts are as follows: Cu_2O–Cl-GLU > Cu_2O–*S*-GLU > Cu_2O–*S*-AA > Cu_2O–Cl-AA, which is consistent with the results of activity test.

Table 3
H_2 consumption of the Cu_2O–Cl-AA, Cu_2O–*S*-AA, Cu_2O–*S*-GLU and Cu_2O–Cl-GLU catalysts obtained from H_2-TPR analysis.

Catalyst	Temperature (°C)			H_2 consumption (mmol/g)			
	α peak	β peak	γ peak	α peak	β peak	γ peak	Total
Cu_2O–Cl-AA	/	326	360	/	3.07	0.82	3.89
Cu_2O–*S*-AA	300	324	352	1.10	2.30	0.97	4.37
Cu_2O–*S*-GLU	250	282	308	3.50	1.29	0.81	5.60
Cu_2O–Cl-GLU	242	286	302	1.22	1.98	1.30	4.50

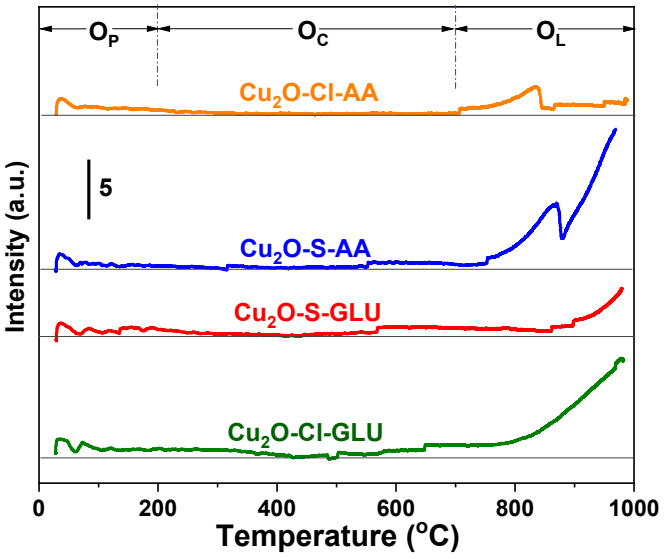

Fig. 6. O_2-TPD profiles of the Cu_2O–Cl-AA, Cu_2O–*S*-AA, Cu_2O–*S*-GLU and Cu_2O–Cl-GLU catalysts. Weight of sample: 50 mg; Gas composition and flow rate: 25% O_2/N_2 mixture (30 mL min^{-1}); Heating rate: 10 °C min^{-1}.

Table 4
The difference of the amount of chemisorbed oxygen among samples[a].

Catalysis / Oxygen Species	Cu_2O–Cl-AA	Cu_2O–*S*-AA	Cu_2O–*S*-GLU	Cu_2O–Cl-GLU
O_P	72.103	70.509	72.584	48.668
O_c	58.940	72.523	161.692	211.088
O_L	192.172	635.312	571.766	697.655
Total	323.215	778.344	806.042	957.411

[a] The calculated area is the absolute area.

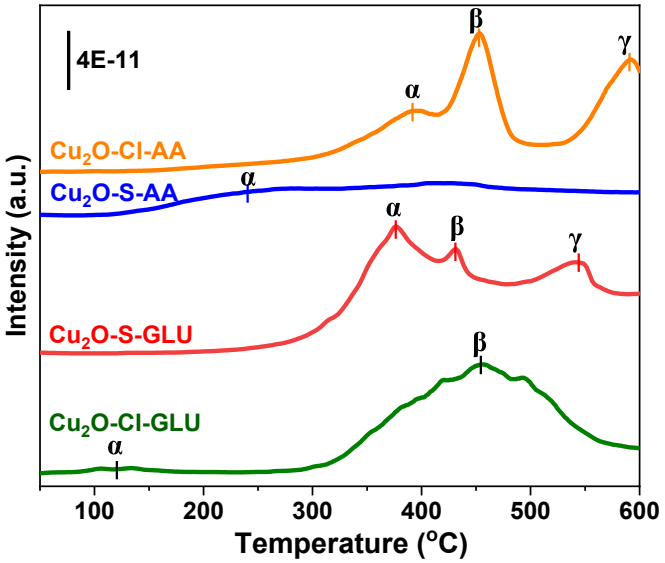

Fig. 7. CO-TPD-MS profiles of the Cu_2O–Cl-AA, Cu_2O–*S*-AA, Cu_2O–*S*-GLU and Cu_2O–Cl-GLU catalysts. Weight of sample: 50 mg; Gas composition and flow rate: high purity CO (99.999%, 30 mL min^{-1}); Heating rate: 10 °C min^{-1}.

3.5. In situ infrared spectrum

In-situ infrared spectra were performed to explore CO adsorption and reaction mechanism during CO oxidation using the Cu_2O–Cl-GLU, as shown in Fig. 8. When pure CO was introduced into the cell for 30 min at room temperature (Fig. 8a and b), the absorption bands at 2172 and 2118 cm^{-1} are assigned to the gaseous CO and adsorbed CO (carbonyls, Cu^+–CO), respectively (Bin et al., 2019; Kang et al., 2022). The adsorbed CO on Cu_2O–Cl-GLU involves an electron donation from carbon (lone pair on 5σ orbital) to d orbitals of the metal cations (Cu^+) and an electron back-donation from d orbitals of the metal cations to 2π*-antibonding of carbon (Wu et al., 2018). The intensity peak for carbonate species, related to interaction of adsorbed CO and O_2 is quite weak at 1400-1800 cm^{-1} due to the absence of gaseous O_2. The in situ infrared spectra are also carried out under the 10% CO+ 21% O_2/Ar continuous stream to identify main active sites during CO oxidation. The IR spectra (Fig. 8c and d) also display intense bands at 2172 and 2118 cm^{-1} assigned to gaseous CO and carbonyls, respectively. When the temperature increases from 30 to 300 °C, the gaseous CO band (2172 cm^{-1}) and carbonyls (2118 cm^{-1}) for the Cu_2O–Cl-GLU reduces rapidly, but the CO_2 bands at 2361, 2342 cm^{-1} grow fast instead, confirming to CO combustion. Owing to the very week interaction of adsorbed CO and O_2 on the Cu_2O surface, the intensity peak for carbonate species were nearly unobserved at 1400-1800 cm^{-1}. As such, the copper sites are available for the transformation and reaction, and become eventually a key aspect in the activity over Cu_2O catalysts.

3.6. Proposed reaction pathway

It is widely accepted that in a typical heterogeneous catalytic reaction, the adsorption of reactants and the activation of adsorbed species are both required for the process to occur (Bin et al., 2014). According to the results mentioned above, the CO self-sustained catalytic combustion over Cu_2O catalysts mainly follows the Mars-van-Krevelen (M-v-K) mechanism, i.e., reaction of adsorbed and activated CO with lattice oxygen. Scheme 2a shows the reaction cycle path of CO on the surface of Cu_2O micro/nanocrystals. There are four elementary reaction steps in the catalytic cycle in Scheme 2a, as shown below:

$$CO + Cu(I) \rightarrow [Cu\text{–}CO] \quad (6)$$

$$[Cu\text{–}CO] + O_L \rightarrow Cu(I) + O_V + CO_2 \quad (7)$$

$$O_2 + O_V \rightarrow O_L + O_C \quad (8)$$

$$[Cu\text{–}CO] + O_C \rightarrow Cu(I) + CO_2 \quad (9)$$

(6) ~ (9) form a catalytic total large cycle, (6) and (7), (6) and (9), (7) and (8) form a small cycle, which promote each other. The activity of lattice oxygen and the amount of chemically adsorbed oxygen directly influence the smooth progress of catalytic reaction. According to the analysis of H_2-TPR, the surface O_L activity of Cu_2O–Cl-GLU and Cu_2O–*S*-GLU is higher than that of Cu_2O–*S*-AA and Cu_2O–Cl-AA, so the oxidation activity of Cu_2O–Cl-GLU and Cu_2O–*S*-GLU to CO is higher than that of Cu_2O–*S*-AA and Cu_2O–Cl-AA. CO adsorbed on Cu(I) reacts with O_L to produce Cu(I), O_V and CO_2. According to the analysis of O_2-TPD profiles, the amount of surface O_C of Cu_2O–Cl-GLU, Cu_2O–*S*-GLU and Cu_2O–*S*-AA is more than that of Cu_2O–Cl-AA. Therefore, the catalytic activity of Cu_2O–Cl-GLU, Cu_2O–*S*-GLU and Cu_2O–*S*-AA is higher than that of Cu_2O–Cl-AA. That is, CO adsorbed on Cu(I) reacts with O_C to yield Cu(I) and CO_2. There is no doubt that the increase of O_V can promote the whole catalytic reaction cycle by accelerating the reaction rate in step (8). From the highly positive correlation between the activity of lattice oxygen and the activity of catalytic reaction, and referring to part of our previous research work (Kang et al., 2018; Ma et al., 2021), it can be inferred that the catalytic reaction of CO on Cu_2O follows the Mars-van-Krevelen (M-v-K) mechanism reaction model

To better understand the content of the conceptual diagram, Scheme 2b is as a diagram of Scheme 2a shows the whole process of CO oxidation on cubic Cu_2O. Firstly, CO is adsorbed on Cu(I), and the active lattice oxygen on the Cu_2O crystal surface reacts with CO generating oxygen vacancy and CO_2, then CO_2 desorbed from the catalyst surface. Subsequently, the gaseous O_2 adsorbed on the oxygen vacancy to supplement O_V to generate O_L and O_C. Due to the exposure rate and coordination unsaturation of atoms increase in the order of face < edge < corner, the catalytic activity of corner is higher than that of edge, and face activity is lowest. Owing to the obvious edge and rough crystal surface of Cu_2O–Cl-GLU, the high exposure rate and coordination unsaturation of atoms in Cu_2O–Cl-GLU lead to high concentration of oxygen vacancies and O_C, which consequently facilitate the CO oxidation activity.

4. Conclusions

Cubic Cu_2O micro/nanocrystals catalysts exposing six (100) crystal planes were successfully prepared with different copper salts and reducing agents of glucose. It is obvious that the effect of reducing agent on the catalytic properties is greater than that of copper salt. The activities of self-sustaining catalytic combustion for high concentration CO decrease in the order of Cu_2O–Cl-GLU > Cu_2O–*S*-GLU > Cu_2O–*S*-AA > Cu_2O–Cl-AA. The reducing agent of glucose can promote the formation of sharper edges and corners, which makes easier for gas-phase oxygen to be activated by lattice oxygen at the sharp edges of the nanocrystals. Meanwhile, compared with ascorbic acid as reductant, the surface of the Cu_2O nanocrystals with glucose as reducing agent is slightly rougher,

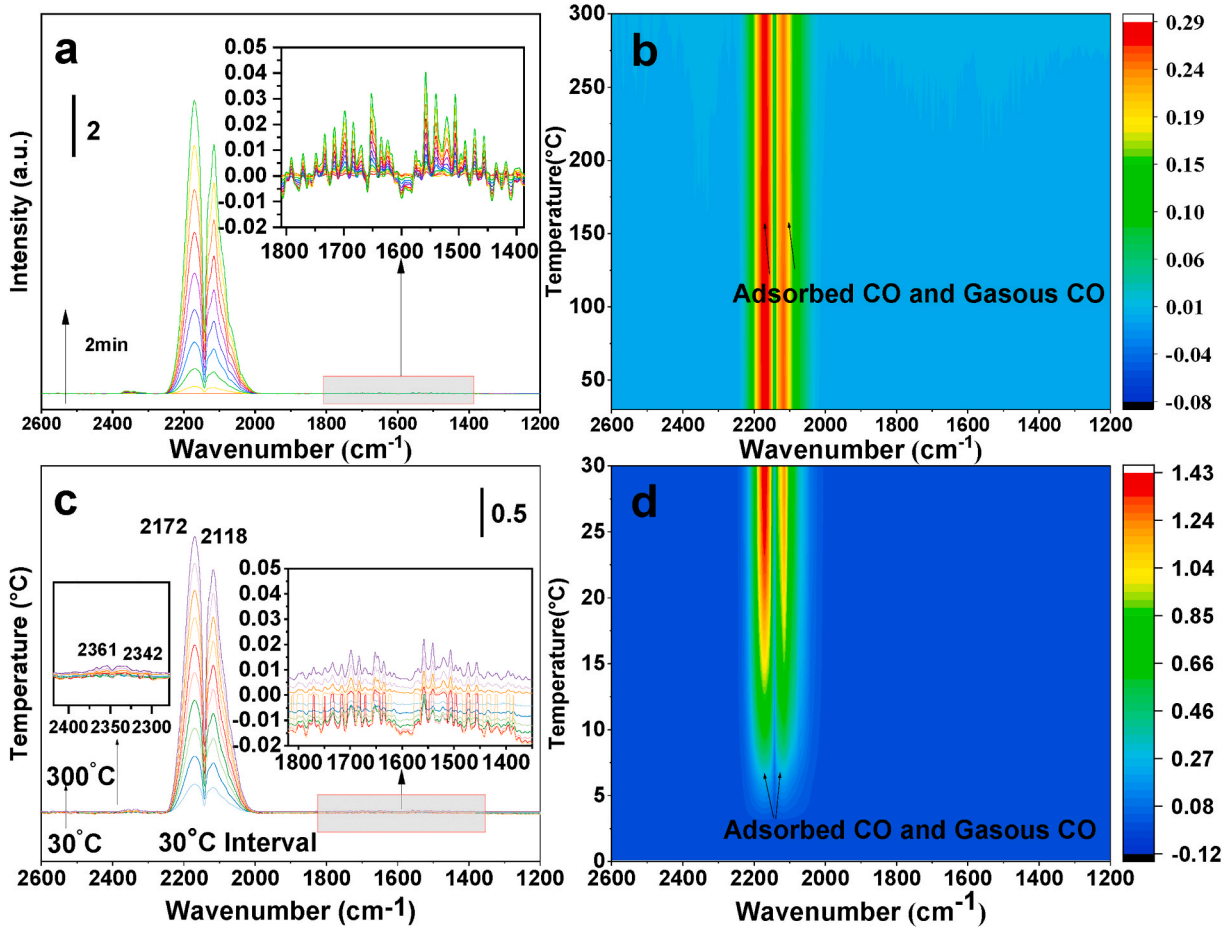

Fig. 8. In situ IR spectra of fresh Cu_2O–Cl-GLU and corresponding mapping results under pure CO (a, b), and 10% CO+ 21% O_2/Ar (c, d) continuous stream.

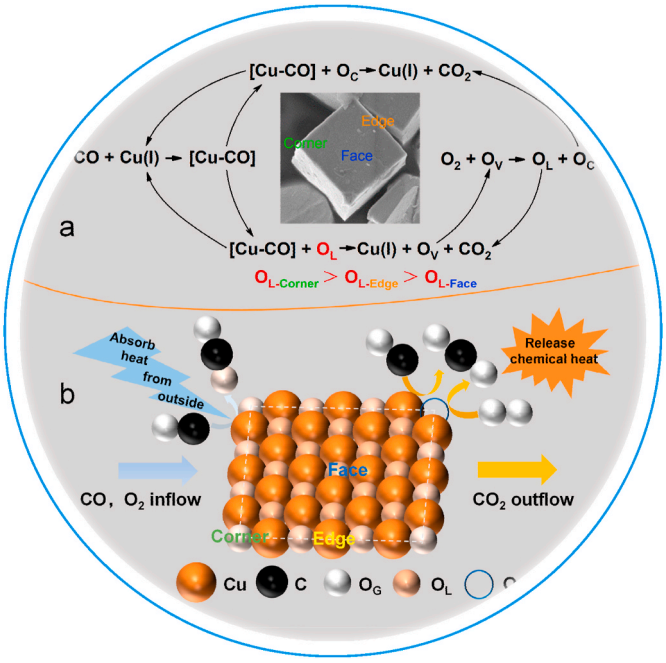

Scheme 2. Cycle path diagram of CO oxidation (a) and schematic diagram of CO oxidation reaction on Cu_2O (b).

which significantly improves the CO oxidation activity. The abundant lattice oxygen that activates gaseous O_2 in the sharp edges, corner of Cu_2O micro/nanocrystals and the step defects and depression defects on the catalyst surface are the main reasons for the improvement of the CO oxidation over Cu_2O–Cl-GLU. Moreover, the high-CO oxidation activity indicates a higher catalytic activity at the corners than that at the edges, with the lowest activity at the faces. The relatively abundant chemisorbed oxygen on the catalyst surface is the key reason for the rapid ignition of CO on the catalyst surface. The study suggests that the glucose is very promising in tuning the surface/interface structure of catalysts.

Author contributions statement

Pandong Ma: Experiment design and execution, catalyst preparation, characterization and activity evaluation, writing of the first draft of the paper. Chenhang Zhang: Reply to the review comments. In situ infrared and first draft experiment design, completion and writing. Baojuan Dou: Writing of the first draft of the paper. Xiaokun Yi: Experiment design, completion and writing. Feng Bin: Provide experimental funds and write the first draft of the thesis. Wenjun Liang: Guide the completion of the experiment and reply to the review comments. Pandong Ma and Chenhang Zhang contributed equally to this work.

Declaration of competing interest

The authors declare that they have no known competing financial interests or personal relationships that could have appeared to influence the work reported in this paper.

Data availability

Data will be made available on request.

Acknowledgments

This work was supported by the Novel Technology of High Efficient Clean Combustion and Energy Saving on Converter Gas (XDA21040500) and the National Natural Science Foundation of China (No. 52176141).

References

Ahmed, I., Zhang, B., Muneeb-Ur-Rehman, M., Fan, W., 2021. Effect of different shapes of Nano-Cu_2O and humic acid on two-generations of Daphnia Magna. Ecotoxicol. Environ. Saf. 207, 111274 https://doi.org/10.1016/j.ecoenv.2020.111274.

Bao, H., Zhang, W., Hua, Q., Jiang, Z., Yang, J., Huang, W., 2011. Crystal-plane-controlled surface restructuring and catalytic performance of oxide nanocrystals. Angew. Chem. 123 (51), 12502–12506. https://doi.org/10.1002/anie.201814258.

Bin, F., Song, C., Lv, G., Song, J., Wu, S., Li, X., 2014. Selective catalytic reduction of nitric oxide with ammonia over zirconium-doped copper/ZSM-5 catalysts. Appl. Catal. B Environ. 150, 532–543. https://doi.org/10.1016/j.apcatb.2013.12.052.

Bin, F., Wei, X., Li, B., San Hui, K., 2015. Self-sustained combustion of carbon monoxide promoted by the Cu-Ce/ZSM-5 catalyst in $CO/O_2/N_2$ atmosphere. Appl. Catal. B Environ. 162, 282–288. https://doi.org/10.1016/j.apcatb.2014.07.007.

Bin, F., Kang, R., Wei, X., Hao, Q., Dou, B., 2019. Self-sustained combustion of carbon monoxide over $CuCe_{0.75}Zr_{0.25}O_\delta$ catalyst: stability operation and reaction mechanism. Proc. Combust. Inst. 37 (4), 5507–5515. https://doi.org/10.1016/j.proci.2018.05.114.

Chang, I.C., Chen, P.C., Tsai, M.C., Chen, T.T., Yang, M.H., Chiu, H.T., Lee, C.Y., 2013. Large-scale synthesis of uniform Cu_2O nanocubes with tunable sizes by in-situ nucleation. CrystEngComm 15 (13), 2363–2366. https://doi.org/10.1039/c3ce26932a.

da Rosa, A.P.P., Cavalcante, R.P., da Silva, D.A., da Silva, L.D.M., da Silva, T.F., Gozzi, F., et al., 2019. H_2O_2-assisted photoelectrocatalytic degradation of Mitoxantrone using CuO nanostructured films: identification of by-products and toxicity. Sci. Total Environ. 651, 2845–2856. https://doi.org/10.1016/j.scitotenv.2018.10.173.

Fan, W., Wang, X., Cui, M., Zhang, D., Zhang, Y., Yu, T., Guo, L., 2012. Differential oxidative stress of octahedral and cubic Cu_2O micro/nanocrystals to Daphnia magna. Environ. Sci. Technol. 46 (18), 10255–10262. https://doi.org/10.1021/es3011578.

Feng, L., Xuan, Z., Bai, Y., Zhao, H., Li, L., Chen, Y., et al., 2014. Preparation of octahedral CuO micro/nanocrystals and electrochemical performance as anode for lithium-ion battery. J. Alloys Compd. 600, 162–167. https://doi.org/10.1016/j.jallcom.2014.02.132.

Ghosh, S., Das, R., Naskar, M.K., 2016. Morphological evolution of hexapod Cu_2O microcrystals by a rapid template-free autoclaving technique. Mater. Lett. 183, 325–328. https://doi.org/10.1016/j.matlet.2016.07.118.

Hua, Q., Cao, T., Bao, H., Jiang, Z., Huang, W., 2013. Crystal-plane-controlled surface chemistry and catalytic performance of surfactant-free Cu_2O nanocrystals. ChemSusChem 6 (10), 1966–1972. https://doi.org/10.1002/cssc.201300376.

Hua, Q., Cao, T., Gu, X.K., Lu, J., Jiang, Z., Pan, X., Huang, W., 2014. Crystal-Plane-Controlled selectivity of Cu_2O catalysts in propylene oxidation with molecular oxygen. Angew. Chem. 126 (19), 4956–4961. https://doi.org/10.1002/ange.201402374.

Ji, S., Chen, Y., Wang, X., Zhang, Z., Wang, D., Li, Y., 2020. Chemical synthesis of single atomic site catalysts. Chem. Rev. 120 (21), 11900–11955. https://doi.org/10.1021/acs.chemrev.9b00818.

Jiang, D., Zhang, Y., Li, X., 2017. Folded-up thin carbon nanosheets grown on Cu_2O cubes for improving photocatalytic activity. Nanoscale 9 (34), 12348–12352. https://doi.org/10.1039/c7nr04364c.

Jiang, W., Ji, W., Au, C.T., 2018. Surface/interfacial catalysis of (metal)/oxide system: structure and performance control. ChemCatChem 10 (10), 2125–2163. https://doi.org/10.1002/cctc.201701958.

Jiao, J., Lin, R., Liu, S., Cheong, W.C., Zhang, C., Chen, Z., Li, Y., 2019. Copper atom-pair catalyst anchored on alloy nanowires for selective and efficient electrochemical reduction of CO_2. Nat. Chem. 11 (3), 222–228. https://doi.org/10.1038/s41557-018-0201-x.

Kang, R., Wei, X., Bin, F., Wang, Z., Hao, Q., Dou, B., 2018. Reaction mechanism and kinetics of CO oxidation over a $CuO/Ce_{0.75}Zr_{0.25}O_{2-\delta}$ catalyst. Appl. Catal. Gen. 565, 46–58. https://doi.org/10.1016/j.apcata.2018.07.026.

Kang, R., Wei, X., Ma, P., Bin, F., He, J., Hao, Q., Dou, B., 2020. Self-sustained combustion of CO with transient changes and reaction mechanism over $CuCe_{0.75}Zr_{0.25}O_\delta$ powder for honeycomb ceramic catalyst. Fuel 263, 116637. https://doi.org/10.1016/j.fuel.2019.116637.

Kang, R., Ma, P., He, J., Li, H., Bin, F., Wei, X., et al., 2021. Transient behavior and reaction mechanism of CO catalytic ignition over a $CuO–CeO_2$ mixed oxide. Proc. Combust. Inst. 38 (4), 6493–6501. https://doi.org/10.1016/j.proci.2020.06.186.

Kang, R., Huang, J., Bin, F., Teng, Z., Wei, X., Dou, B., Kasipandi, S., 2022. Evolution behavior and active oxygen quantification of reaction mechanism on cube Cu_2O for CO self-sustained catalytic combustion and chemical-looping combustion. Appl. Catal. B Environ. 310, 121296 https://doi.org/10.1016/j.apcatb.2022.121296.

Karapetyan, A., Reymers, A., Giorgio, S., Fauquet, C., Sajti, L., Nitsche, S., et al., 2015. Cuprous oxide thin films prepared by thermal oxidation of copper layer. Morphological and optical properties. J. Lumin. 159, 325–332. https://doi.org/10.1016/j.jlumin.2014.10.058.

Kumar, V.V., Dharani, A., Mariappan, M., Anthony, S.P., 2016. Synthesis of CuO and Cu_2O nano/microparticles from a single precursor: effect of temperature on CuO/Cu_2O formation and morphology dependent nitroarene reduction. RSC Adv. 6 (88), 85083–85090. https://doi.org/10.1039/C6RA16553B.

Li, R., Yan, X., Yu, L., Zhang, Z., Tang, Q., Pan, Y., 2013. The morphology dependence of cuprous oxide and its photocatalytic properties. CrystEngComm 15 (46), 10049–10058. https://doi.org/10.1039/c3ce41470a.

Liang, X., Gao, L., Yang, S., Sun, J., 2009. Facile synthesis and shape evolution of single-crystal cuprous oxide. Adv. Mater. 21 (20), 2068–2071. https://doi.org/10.1002/adma.200802783.

Liu, H., Zhou, Y., Kulinich, S.A., Li, J.J., Han, L.L., Qiao, S.Z., Du, X.W., 2013. Scalable synthesis of hollow Cu_2O nanocubes with unique optical properties via a simple hydrolysis-based approach. J. Mater. Chem. 1 (2), 302–307. https://doi.org/10.1039/c2ta00138a.

Luo, X.L., Wang, M.J., Yang, D.S., Yang, J., Chen, Y.S., 2015. Hydrothermal synthesis of morphology controllable Cu_2O and their catalysis in thermal decomposition of ammonium perchlorate. J. Ind. Eng. Chem. 32, 313–318. https://doi.org/10.1016/j.jiec.2015.09.015.

Ma, P., Teng, Z., Hao, Q., Kang, R., Li, B., Bin, F., Dou, B., 2021. Effects of precursor concentration on morphologies of Cu_2O micro/nanocrystals and properties of CO self-sustained catalytic combustion. Fuel 289, 119776. https://doi.org/10.1016/j.fuel.2020.119776.

Muthukumaran, M., Niranjani, S., Barnabas, K.S., Narayanan, V., Raju, T., Venkatachalam, K., 2019. Green route synthesis and characterization of cuprous oxide (Cu_2O): visible light irradiation photocatalytic activity of MB dye. Mater. Today Proc. 14, 563–568. https://doi.org/10.1016/j.matpr.2019.04.179.

Ng, S.Y., Ngan, A.H.W., 2013. One-and two-dimensional cuprous oxide nano/micro structures fabricated on highly orientated pyrolytic graphite (Hopg) by electrodeposition. Electrochim. Acta 114, 379–386. https://doi.org/10.1016/j.electacta.2013.10.067.

Park, J.C., Kim, J., Kwon, H., Song, H., 2009. Gram-scale synthesis of Cu_2O nanocubes and subsequent oxidation to CuO hollow nanostructures for lithium-ion battery anode materials. Adv. Mater. 21 (7), 803–807. https://doi.org/10.1002/adma.200800596.

Qin, C., Chen, X., Liang, R., Jiang, N., Zheng, Z., Ye, Z., Zhu, L., 2022. Fabricating high-quality Cu_2O photocathode by magnetron sputtering: insight into defect states and charge carrier collection in Cu_2O. ACS Appl. Energy Mater. https://doi.org/10.1021/acsaem.2c02974.

Rao, R., Liang, H., Hu, C., Dong, H., Dong, X., Tang, Y., Fong, S., Liang, Q., 2022. Enhancing catalytic performance of Ag-CeO_2 catalysts for catalytic CO combustion: Ag-CeO_2 interface interaction and Na-promoting action. Fuel 317. https://doi.org/10.1016/j.fuel.2022.123439.

Shang, Y., Sun, D., Shao, Y., Zhang, D., Guo, L., Yang, S., 2012. A facile top-down etching to create a Cu_2O jagged polyhedron covered with numerous {110} edges and {111} corners with enhanced photocatalytic activity. Chem.–Eur. J. 18 (45), 14261–14266. https://doi.org/10.1002/chem.201201882.

Shang, H., Zhou, X., Dong, J., Li, A., Zhao, X., Liu, Q., Li, Y., 2020. Engineering unsymmetrically coordinated Cu-S1N3 single atom sites with enhanced oxygen reduction activity. Nat. Commun. 11 (1), 1–11. https://doi.org/10.1038/s41467-020-16848-8.

Shi, H., Yu, K., Wang, Y., Wang, Q., Zhu, Z., 2012. Shape evolution, photoluminescence and degradation properties of novel Cu_2O micro/nanostructures. Appl. Phys. A 108 (3), 709–717. https://doi.org/10.1007/s00339-012-6954-y.

Wu, L., Zhang, L., Xun, Z., Yu, G., Shi, L., 2016. Effect of growth temperature and time on morphology and gas sensitivity of Cu_2O/Cu microstructures. J. Nanomater. https://doi.org/10.1155/2016/4580518, 2016.

Wu, Y., Li, L., Chu, B., Yi, Y., Qin, Z., Fan, M., Dong, L., 2018. Catalytic reduction of NO by CO over B-site partially substituted $LaM_{0.25}Co_{0.75}O_3$ (M= Cu, Mn, Fe) perovskite oxide catalysts: the correlation between physicochemical properties and catalytic performance. Appl. Catal. Gen. 568, 43–53. https://doi.org/10.1016/j.apcata.2018.09.022.

Xu, J.F., Ji, W., Shen, Z.X., Tang, S.H., Ye, X.R., Jia, D.Z., Xin, X.Q., 1999. Preparation and characterization of CuO nanocrystals. J. Solid State Chem. 147 (2), 516–519. https://doi.org/10.1006/jssc.1999.8409.

Xu, B., Zhou, J., Ni, Z., Zhang, C., Lu, C., 2018. Synthesis of novel microencapsulated phase change materials with copper and copper oxide for solar energy storage and photo-thermal conversion. Sol. Energy Mater. Sol. Cell. 179, 87–94. https://doi.org/10.1016/j.solmat.2018.02.008.

Yang, T., Li, K., Liu, Z., Pu, L., Zhang, X., 2017. One-step synthesis of hydrangea-like Cu_2O@ N-doped activated carbon as air cathode catalyst in microbial fuel cell. J. Electrochem. Soc. 164 (4), F270. https://doi.org/10.1149/2.0401704jes.

Yang, Y., Xu, C., Yan, J., Liu, F., Li, L., 2022. Reaction mechanism and micro kinetics of CO catalytic combustion over Ni-doped $LaCoO_3$ perovskite. Proc. Combust. Inst. 7, 16. https://doi.org/10.1016/j.proci.2022.06.023.

Yoon, S., Kim, S.D., Choi, S.Y., Lim, J.H., Yoo, B., 2015. Hierarchical shape evolution of cuprous oxide micro-and nanocrystals by surfactant-assisted electrochemical deposition. Cryst. Growth Des. 15 (10), 4969–4974. https://doi.org/10.1021/acs.cgd.5b00873.

Zhang, Z., Wu, H., Yu, Z., Song, R., Huang, W., 2019a. Site-Resolved Cu_2O catalysis in the oxidation of CO. Angew. Chem. 58 (13), 4276–4280. https://doi.org/10.1002/anie.201814258.

Zhang, Z., Wu, H., Yu, Z., Song, R., Qian, K., Chen, X., et al., 2019b. Site-resolved Cu_2O catalysis in the oxidation of CO. Angew. Chem. 58 (13), 4276–4280. https://doi.org/10.1002/anie.201814258.

Zhu, Q., Zhang, Y., Wang, J., Zhou, F., Chu, P.K., 2011. Microwave synthesis of cuprous oxide micro-/nanocrystals with different morphologies and photocatalytic activities. J. Mater. Sci. Technol. 27 (4), 289–295. https://doi.org/10.1016/S1005-0302(11)60064-9.